AGU PUBLICATIONS

Journal of Advances in Modeling Earth Systems

RESEARCH ARTICLE
10.1002/2014MS000342

Large-scale character of an atmosphere in rotating radiative-convective equilibrium

Xiaoming Shi[1] and Christopher S. Bretherton[1]

[1]Department of Atmospheric Sciences, University of Washington, Seattle, Washington, USA

Key Points:
- Multiple tropical cyclone-like vortices coexist in rotating RCE on a sphere
- Self-aggregation and baroclinic instability limit the spacing of vortices
- The tropics is dominated by a Hadley circulation driven by eddy momentum flux

Correspondence to:
X. Shi,
shixm@atmos.washington.edu

Citation:
Shi, X., and C. S. Bretherton (2014), Large-scale character of an atmosphere in rotating radiative-convective equilibrium, *J. Adv. Model. Earth Syst.*, *06*, doi:10.1002/2014MS000342.

Received 1 MAY 2014
Accepted 21 JUN 2014
Accepted article online 26 JUN 2014

Abstract A rotating radiative-convective equilibrium on a sphere is reached using a global atmospheric model with prescribed globally uniform sea surface temperature and no insolation. In such an equilibrium state, multiple tropical cyclone-like vortices coexist in the extratropics, moving slowly poleward and westward. Many vortices have a lifetime longer than 2 months and travel from the tropics to the polar regions. The typical spacing of simulated tropical cyclone-like vortices is comparable to the deformation radius, while the production of available potential energy is at a scale slightly smaller than those vortices. It is hypothesized that the growth of tropical cyclone-like vortices is driven by the self-aggregation of convection, while baroclinic instability destabilizes any vortices that grow significantly larger than the deformation radius. A weak Hadley circulation dominates in the deep tropics, and an eastward propagating wave number 1 Kelvin-like mode having a period of 30–40 days develops at the equator. The weak Hadley circulation is found to emerge from an initially quiescent atmosphere due to poleward momentum transport by the vortices.

1. Introduction

As stated by *Bretherton et al*. [2005], radiative-convective equilibrium (RCE) in a nonrotating, horizontally homogeneous environment is a time-honored idealization for understanding the tropical atmosphere and its sensitivity to relevant forcings. Its history can be traced back to the early work by *Manabe and Strickler* [1964] with single-column models. Modern RCE simulations employ cloud-resolving models to study a wide number of issues, including controls on the hydrological cycle [*Romps*, 2011], the distribution of convective mass fluxes [*Tompkins and Craig*, 1998], scaling laws for moist convection [*Robe and Emanuel*, 1996], etc.

Recently, *Held and Zhao* [2008] proposed RCE in a rotating environment, simulated using general circulation models (GCMs), as a useful framework for studying the tropical cyclones (TCs) produced by global models. Recent studies suggest that atmospheric resolutions in the range of 20–100 km may be sufficient to study many aspects of TCs [*Zhao et al*., 2009]. Idealized experiments can illuminate the influence of external parameters and model assumptions on TC simulations. Rotating RCE simulations described by *Held and Zhao* [2008] used the column physics of GFDL's Atmospheric Model 2 (AM2) and a hydrostatic dynamical core in a doubly periodic box. In their large 2×10^4 km square horizontally homogeneous domain with fixed sea surface temperature (SST) and uniform Coriolis parameter f, multiple TCs coexist in the equilibria reached by their simulations. Increasing SST made the number of TCs decrease in their simulations while the average intensity increased. The spacing between TCs was found to be inversely proportional to f.

A new variant of rotating RCE was developed by *Khairoutdinov and Emanuel* [2013] using a cloud-resolving model in a small 2300 km square domain. In order to allow multiple TCs to coexist in their small domain, they artificially increased the Coriolis parameter from typical values in the tropics by about 1 order of magnitude. Besides finding similar dependence of TC size and intensity on SST, they also found that the outflow temperature of TC's remains relatively invariant with SST, consistent with the Fixed Anvil Temperature (FAT) hypothesis proposed by *Hartmann and Larson* [2002] for tropical deep convection.

However, for realistic values of the Coriolis parameter, cloud-resolving resolution simulations in a small domain usually only allow one TC to develop [e.g., *Nolan et al*., 2007; *Nolan and Rappin*, 2008]. The small domain size is a strong constraint on simulated TCs and the horizontal mean equilibrium state they help to create. Indeed, *Zhou et al*. [2014] explored the dependence of the equilibrium state upon domain size using a model similar to *Held and Zhao* [2008]. They found that as domain size increases, the equilibrium evolves

through four regimes: a single tropical depression, an intermittent tropical cyclone with widely varying intensity, a single sustained storm, and finally multiple storms.

In this paper, we document the major characteristics of the large-scale flow in rotating RCE using a model similar to that of *Held and Zhao* [2008], but on a spherical earth. Such experiments help bridge between the TCs in even more idealized simulations and real-world simulations.

Our simulation is not the first to explore RCE on a rotating sphere, but probably due to inadequate horizontal resolution, TCs were absent in earlier simulations of rotating RCE on a sphere. Previous work focused on an ITCZ that forms spontaneously in rotating RCE on a sphere. *Sumi* [1992] described how the ITCZ forms with particular emphasis on the evolution of convective activity. *Kirtman and Schneider* [2000] provided more detailed analysis of the general circulation in similar experiments, pointing out that the easterlies within the ITCZ and westerlies in the subtropics of the aquaplanet in rotating RCE implied poleward transport of angular momentum in those simulations. Such an ITCZ also exists in our simulations and will be discussed later in the paper.

Our analysis and discussion will primarily focus on the characteristics of atmospheric dynamics associated with TC-like vortices (TCLVs) in rotating RCE. General circulation features of the simulated ITCZ will also be discussed and compared with the previous literature, so as to provide a complete picture of the atmospheric motions in rotating RCE on a sphere.

2. Model Information

The GCM used in this study is the global atmosphere model AM2.1, developed by the Geophysical Fluid Dynamics Laboratory (GFDL) [*Anderson et al*., 2004]. Standard physics schemes and parameters of AM2.1 are adopted in our simulations unless otherwise specified in the following text. A brief description of AM2.1 model components is given below. Readers interested in details of AM2.1 physics schemes or dynamics are referred to *Anderson et al*. [2004, and references therein].

AM2.1 has a finite-volume dynamical core on a latitude-longitude grid [*Lin*, 2004], which in our simulations has a resolution of 1° latitude by 1.25° longitude, with 24 vertical levels. The whole planet is covered by ocean with a fixed uniform sea surface temperature (SST) of 300 K.

As detailed in *Anderson et al*. [2004], grid-resolved clouds and precipitation in AM2.1 are parameterized with the aid of prognostic variables for the cloud fraction and the specific humidities of cloud liquid water and cloud ice. Grid-scale fluxes of rain and snow are computed diagnostically from these prognostic fields [*Rotstayn*, 1997; *Rotstayn et al*., 2000]. Cumulus convection is represented by the Relaxed Arakawa-Schubert formulation of *Moorthi and Suarez* [1992].

The long-wave radiation code of AM2.1 accounts for the absorption and emission by the principal gases in the atmosphere, including H_2O, CO_2, O_3, N_2O, CH_4, and halocarbons. The concentrations of those gases are fixed at climatological means, and the radiative effects of aerosols are not included in these simulations. Solar radiation is also eliminated.

We first run a simulation starting from the observed atmospheric state of the Earth on a random day for 3 years, during which an equilibrium state is already achieved. Yet, in order to make sure this equilibrium state is not directly influenced by its particular initial condition, we take the last month's globally averaged profiles of temperature and moisture and global mean surface pressure to create a new initial condition, in which wind velocity is set to zero everywhere. Then we run the model for another 3 years and discard the first 2 years as spin-up. As expected, this new simulation reaches the same equilibrium state as before in less than 1 year. Our analysis below uses averages over the last year's data of this simulation unless otherwise specified.

3. TC-Like Vortices

The most prominent feature of the atmospheric motions in the rotating RCE state is the existence of many TC-like vortices (TCLVs) throughout the extratropical atmosphere, at latitudes roughly poleward of 10° (Figure 1). The vortices in the northern (southern) hemisphere in general move slowly northwestward (southwestward), and many of them have very long lifetimes.

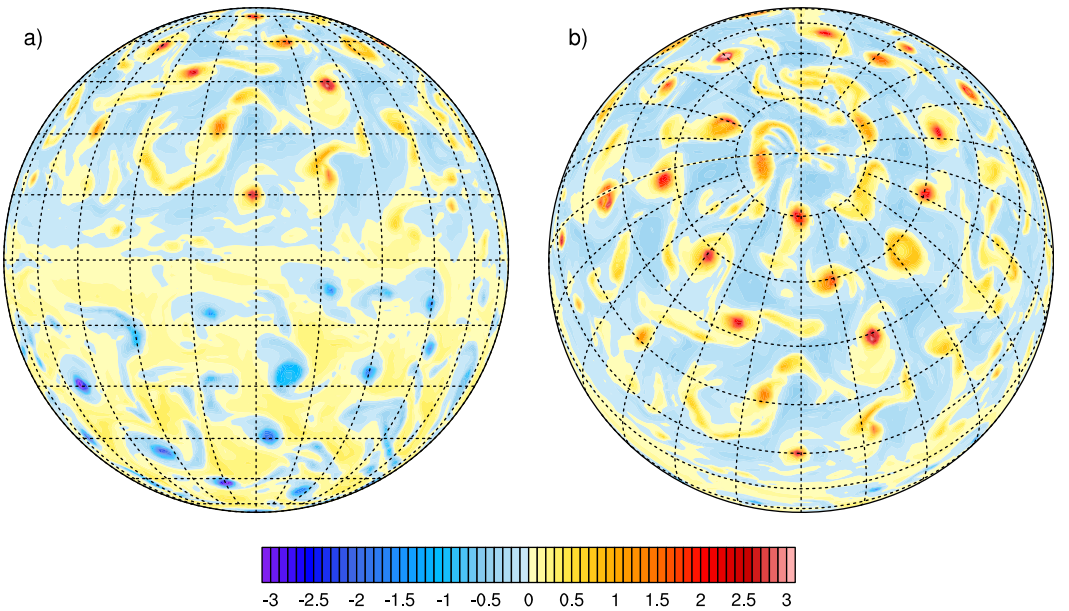

Figure 1. Instantaneous distribution of relative vorticity (10^{-4} s^{-1}) at 850 hPa level. (a and b) The same field viewed from different angles.

We identify and track individual TCLVs in the simulation using 6 h data of the 850 hPa relative vorticity field. All data are smoothed horizontally with a Gaussian filter first to remove small-scale "noise." Each individual TC-like vortex in the northern (southern) hemisphere is defined as a continuous region with positive (negative) vorticity and minimum value greater than $3\times10^{-5}s^{-1}$ (less than $-3\times10^{-5}s^{-1}$). By this standard, the temporally averaged number of TCLVs on each hemisphere is about 36. The center of each vortex is calculated as the vorticity-weighted mean coordinate of this positive (negative) vorticity patch, while its "radius" r is defined as the maximum distance between its center and border. Finally if vortex j among all vortices at time step $n+1$ is closest to vortex i at the 6 h earlier time step n and if the distance between their centers is less than both their diameters $2r_i$ and $2r_j$, we merge vortex j and i into a single vortex, which we track at later time steps.

In the Northern Hemisphere, most of the trajectories found by the above procedure show a southeast-northwest orientation, especially the longer ones. Figure 2 shows the trajectories of vortices that moved more than 45° latitude in the meridional direction. While some of those trajectories are wobbling or cycloidal, they all move poleward and westward in the end. There are 176 such long trajectories globally in the 1 year simulation data. Their average duration is 60 days, and the longest one is 120 days. Figure 3 shows the averaged trajectory of 57 TCLVs from both hemispheres starting from latitudes lower than 15° and ending at least 60° poleward of their initial positions. Shorter trajectories are discarded for ease in calculating the mean trajectory. At its poleward edge, the mean trajectory breaks up into little pieces, because TCLVs tend to swirl in place when they are near the pole and thus lose consistency in their direction of motion.

The poleward and westward movement of TCLVs can be explained by the beta effect on tropical cyclone motion (beta drift) [e.g., *Chan and Williams*, 1987; *Wang and Li*, 1992; *Li and Wang*, 1994; *Wang and Holland*, 1996]. An initially symmetric vortex in the Earth's vorticity gradient will develop a pair of counter-rotating gyres due to Rossby wave dispersion. These asymmetric gyres induce a relative flow across the vortex core causing it to propagate poleward and westward [*Wang and Holland*, 1996]. *Li and Wang* [1994] found that depending on initial vortex structure, the vortex may follow a variety of tracks ranging from a quasi-steady displacement to a wobbling, or a cycloidal track due to the evolution of the asymmetric gyres. This is consistent with the complex details of the TCLV tracks in Figure 2.

4. Energy Spectrum

Driven by convective instability and constrained by the rotation of the planet, the large-scale circulation in rotating RCE is ultimately a problem in geostrophic turbulence. In this section, we examine the energy spectrum in this light. In our simulation, the barotropic circulation, which is defined as the vertically averaged

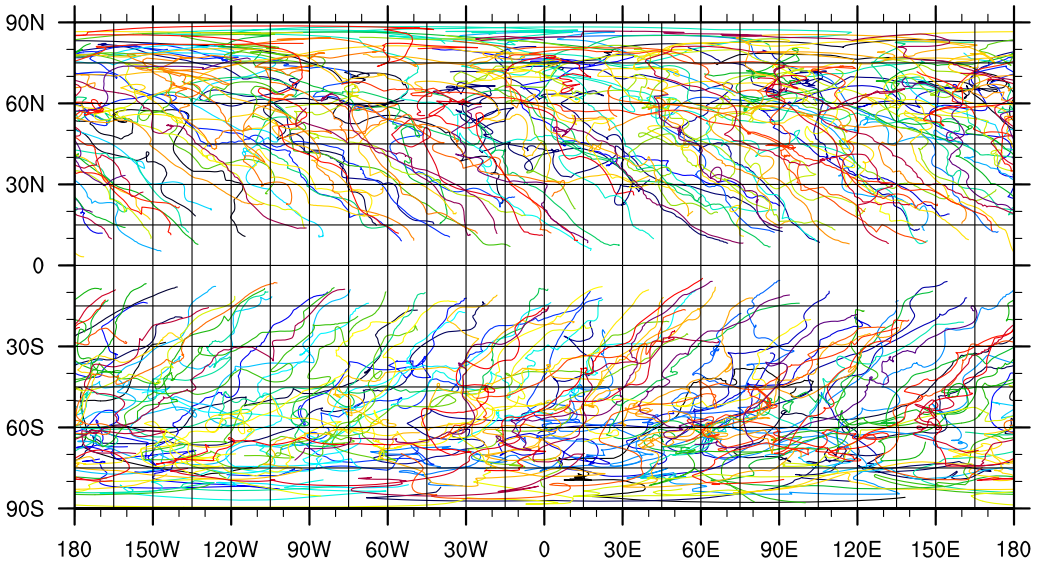

Figure 2. Trajectories of vortices that moved more than 45° latitude in the meridional direction.

component of atmospheric motions, contains about 80% of the total available potential energy (APE) and about 75% of the total kinetic energy (KE) of the circulation. Hence, we will focus hereafter on the barotropic energy spectrum.

Our calculation of KE and APE spectra follow the formulation of *Augier and Lindborg* [2013]. The globally integrated barotropic KE and APE are

$$E_K = \frac{p_s - p_t}{g} \int \left(\frac{u_m^2 + v_m^2}{2} \right) a^2 d\Omega, \quad (1)$$

$$E_A = \frac{p_s - p_t}{g} \int \left(\gamma \frac{\theta_m'^2}{2} \right) a^2 d\Omega, \quad (2)$$

respectively. These are areal integrals around the globe, where $d\Omega$ is an infinitesimal element of solid angle, a is the radius of the Earth, p_s and p_t are the mean surface and tropopause pressure where $p_t \approx 250$hPa in our simulations, u_m and v_m are the barotropic velocity components, while θ'_m is the barotropic component of the deviation of potential temperature from its mean profile. Strictly speaking, γ, which is related to the mean stratification, is a function of pressure. But in our simulations, it is nearly a constant in the free troposphere, thus we use its mean value, 8Jkg^{-1}K^{-2}, in our

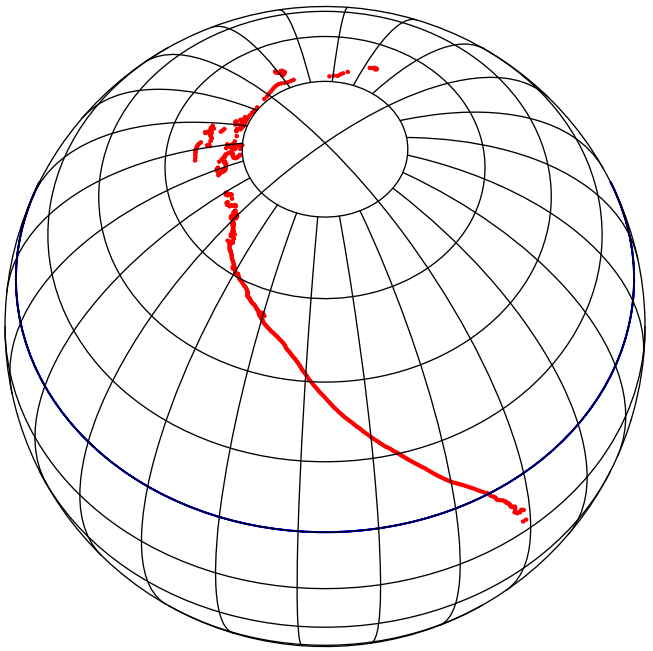

Figure 3. Averaged trajectory of long-lived vortices starting from latitudes lower than 15° and ending at least 60° poleward of their initial positions. The latitude circle in blue indicates 15°N.

calculation. The globally integrated barotropic KE and APE are 7.2×10^{19} J and 5.2×10^{19} J, respectively, in our simulation.

Similar to *Augier and Lindborg* [2013], we calculate the energy spectrum of the global atmosphere using spherical harmonics Y_{lm}. The spectral components of KE and APE are defined as follows:

$$E_K^{lm} = \frac{a^4}{2l(l+1)}\left(\hat{\zeta}_{lm}\hat{\zeta}_{lm}^* + \hat{\mathcal{D}}_{lm}\hat{\mathcal{D}}_{lm}^*\right), \tag{3}$$

$$E_A^{lm} = \frac{a^2\gamma}{2}\hat{\theta}_{lm}\hat{\theta}_{lm}^*, \tag{4}$$

where $\hat{\zeta}_{lm}$, $\hat{\mathcal{D}}_{lm}$, and $\hat{\theta}_{lm}$ are the spectral coefficients of vorticity, divergence, and potential temperature disturbance, respectively. Since the total wave number of spherical harmonics is $k=\sqrt{l(l+1)}/a$, we further sum up spectral functions with respect to zonal wave number to obtain the energy spectra with respect to total wave number:

$$E_K^l = \sum_{|m|\le l} E_K^{lm}, \tag{5}$$

$$E_A^l = \sum_{|m|\le l} E_A^{lm}. \tag{6}$$

Figure 4 shows the spectrum of KE, APE, and KE+APE. The spectrum of total energy (KE+APE) has a k^{-3} spectral slope in intermediate wave numbers and drops off more steeply at large wave numbers. Throughout this range, it is dominated by KE. The APE spectrum, which is roughly only 1/5 of the KE spectrum in strength at intermediate wave numbers, has a k^{-4} spectral slope. The spectrum of both KE and APE is flat for $l \le 16 (k < k_c = 16.5/a)$. This cutoff scale corresponds to a half-wavelength of 1200 km, which is approximately equal to the midlatitude dry deformation radius, $L_d = NH/f_0 \approx 1100$ km, where $N^2 = 1.25\times10^{-4}\mathrm{s}^{-2}$, $H = 10$ km for our simulation.

Held and Zhao [2008] suggested that the spacing between vortices may scale with L_d, consistent with the cutoff wave number in our energy spectra. In our simulations, N and H are nearly uniform around the globe so L_d is proportional to $1/f$. We can calculate the TCLV spacing in each latitude band based on the number of vortices per unit area. We divide the whole planet into 15° wide latitude bands and denote the time mean of TC numbers in a given band by $\bar{N}$. The characteristic diameter of influence of TCLVs in each band is defined by $L_v = 2\sqrt{S_\varphi/(\pi\bar{N})}$, where S_φ is the area of the latitude band centered at latitude φ.

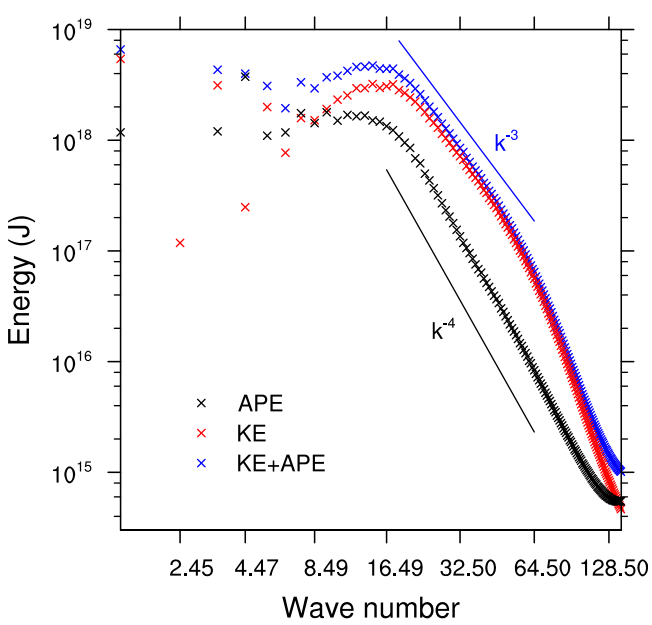

Figure 4. Energy spectrum of globally integrated barotropic KE, APE, and KE+APE.

The characteristic diameters of influence of TCLVs at different latitude bands are plotted in Figure 5 as red dots. They are roughly proportional to the change in $1/f$ and hence L_d with respect to latitude. In the extratropics, L_v is approximately 2 L_d.

5. Scale of Energy Production

The above characteristics of the atmosphere in rotating RCE, namely, the k^{-3} spectral slope and the spectral peak at

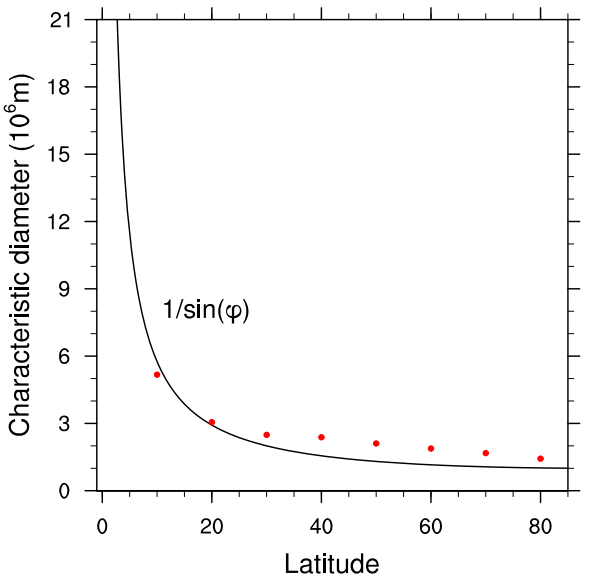

Figure 5. Characteristic diameters of influence of vortices versus latitude.

the scale of the deformation radius, are surprisingly similar to observations of the Earth's atmosphere. At scales smaller than the deformation radius, the energy spectrum of the Earth's atmosphere follows an approximate −3 law [e.g., *Gage and Nastrom*, 1986]. At scales larger than the deformation radius the spectrum is somewhat flat and uneven, with no distinct slope [e.g., *Augier and Lindborg*, 2013].

In the case of the Earth's atmosphere, the spectral slope changes near the scale of the deformation radius because L_d is the scale at which energy is injected into the barotropic mode through processes associated with baroclinic instability [*Salmon*, 1978, 1980; *Zurita-Gotor and Vallis*, 2009]. A k^{-3} spectral slope forms at scales smaller than L_d as a result of the downscale enstrophy cascade in two-dimensional geostrophic turbulence.

In rotating RCE, energy is also injected into barotropic eddy motions at the scale L_d, but via a totally different mechanism involving latent heating, as we now show. We calculate the power spectrum of APE generation rate due to diabatic heating in our simulation. The APE generated by diabatic heating at a grid point is [*Augier and Lindborg*, 2013]

$$G(p,\varphi,\lambda)=\gamma\overline{\theta' Q'_\theta}, \tag{7}$$

where θ' is potential temperature fluctuation, Q_θ is the tendency of potential temperature due to diabatic heating (radiation and latent heat release), and Q'_θ is the deviation from its time mean, p, φ, λ are pressure, latitude, and longitude, respectively. By integrating G vertically and using spherical harmonics, we get the power spectrum of APE generation rate due to diabatic heating (Figure 6).

Comparison of Figures 5 and 6 tells us that most of the diabatic heating term, which is mainly due to latent heat release, concentrates at scales slightly smaller than the scale of vortices, which is not surprising, since the diabatic heating perturbations are concentrated in the cores of the vortices. APE generation in the simulations is stronger in the upper troposphere than at lower levels and maximizes near the 300 hPa pressure level.

Figure 7 shows an instantaneous distribution of vertically integrated G, overlaid with contours of surface pressure anomaly. A mature TCLV has strong production of APE by diabatic heating right above its surface low-pressure center, collocated with the surface vorticity maximum, and a broader region of very weak APE dissipation surrounds it.

Therefore, the atmosphere in rotating RCE has maximum energy production at scales comparable to the deformation radius, and this is why it has an energy spectrum similar to that of the Earth's atmosphere.

One may ask why the spacing of TCLVs, and thus the scale of its energy production, is not significantly smaller, or larger, than the scale of the deformation radius. The growth of TCLVs at small scales may be explained by the self-aggregation of convection [*Bretherton et al*., 2005; *Muller and Held*, 2012]. Three-dimensional cloud-resolving simulations by *Bretherton et al*. [2005] show that an upgradient transport of moist static energy exists in the aggregated state, with moist static energy transported from low-energy (dry) to high-energy (moist) regions.

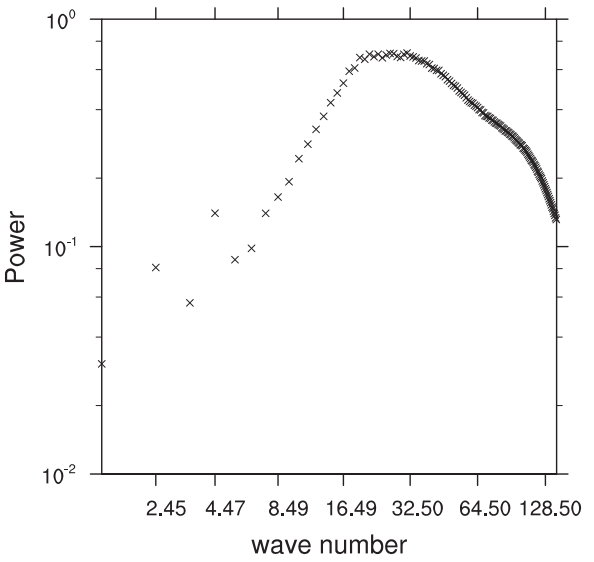

Figure 6. Power spectrum of vertically integrated APE generation rate due to diabatic heating.

Figure 8 shows the development of precipitation and water vapor path (WVP) in the first 16 days of our simulation. One can find two initial growth modes in Figure 8. One originates from a few strong WVP anomalies that are already apparent at day 2, the other develops from random convection that becomes prominent a few days later. Both modes grow upscale with time, and the overall distribution of WVP and precipitation becomes better organized at day 16. The evolution of the second mode suggests that random convection initially at very small scales can self-aggregate to the deformation radius; hence, in the equilibrium of rotating RCE, TCLVs will grow to at least this scale.

The strong initial WVP anomalies of the first mode grow to large vortices at day 10. But at day 13 and 16, those large vortices split into smaller ones, suggesting that TCLVs of their size are not stable. We now argue that baroclinic instability may be the cause.

Figure 9 shows an instantaneous distribution of the differential wind speed between 250 and 850 hPa, $|\mathbf{V}_{250}-\mathbf{V}_{850}|$, and the anomalous temperature field at 500 hPa. The horizontal temperature gradient between the warm cores of TCLVs and the surrounding regions is ∼5K per 10° of longitude/latitude, which is comparable with the meridional temperature gradient of Earth's atmosphere. The temperature gradient is weaker at lower levels, but at 850 hPa level, it is still greater than 3 K per 10° of longitude/latitude. Thermal wind balance requires a vertical wind shear between upper and lower troposphere levels that can exceed 20 m s^{-1}, which is also of comparable size to vertical wind shear at midlatitudes of the Earth.

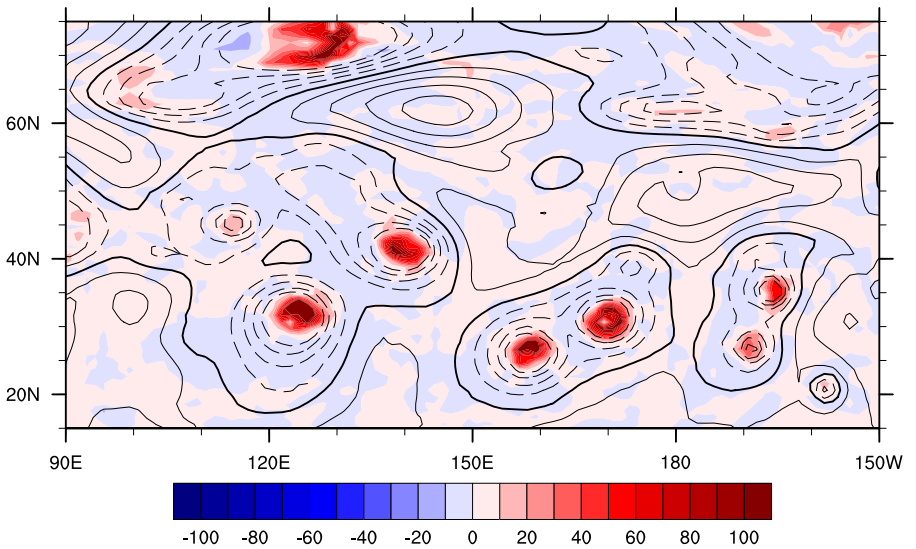

Figure 7. A snapshot of vertically integrated APE generation rate (color, in Wm^{-2}) due to diabatic heating, and the corresponding surface pressure anomaly (contours with 2 hPa intervals). The thick solid contour is indicating zero, negative pressure anomaly is contoured in dash lines, and positive values are in solid thin lines.

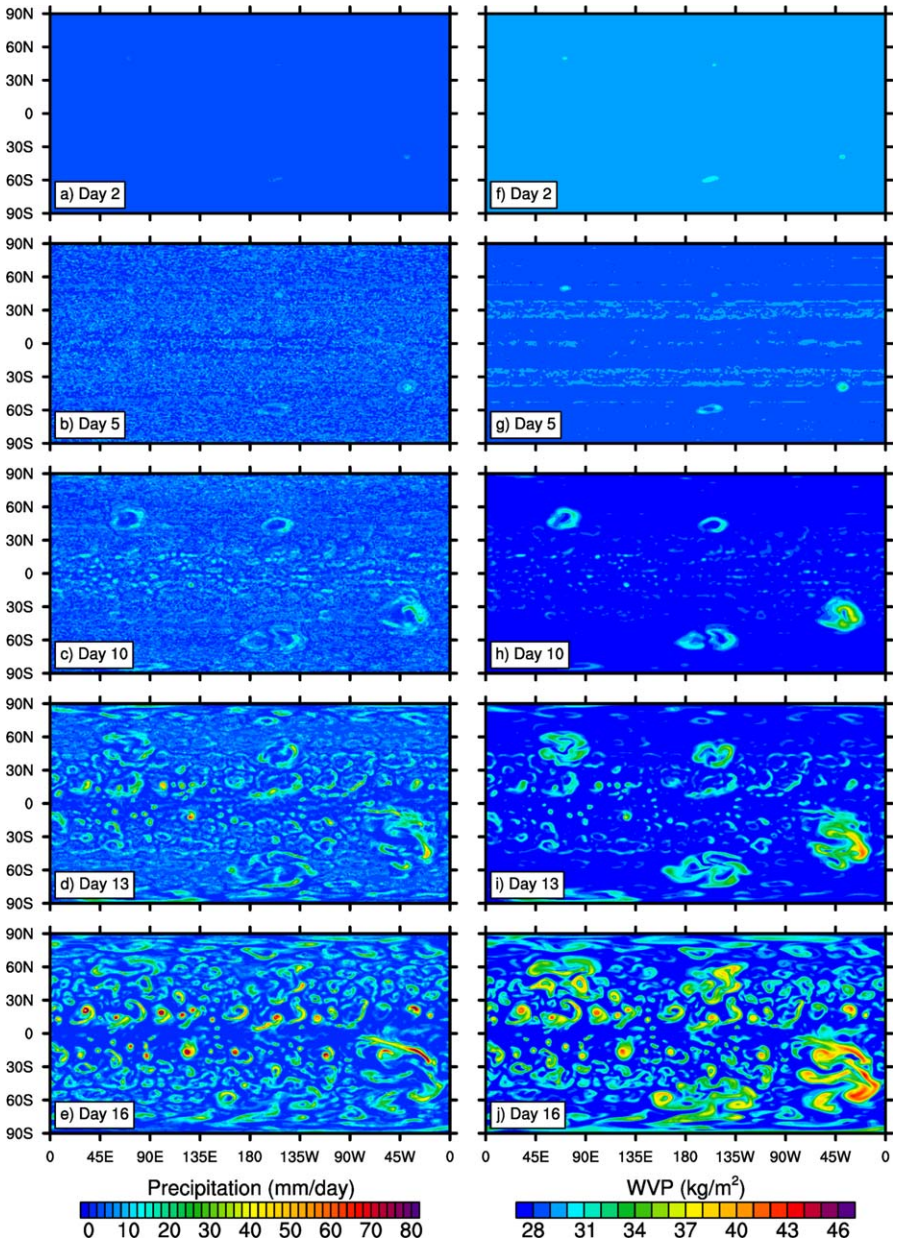

Figure 8. (left) Development of daily mean precipitation and (right) water vapor path (WVP) in the first 16 days of the simulation.

Therefore, it is plausible to think baroclinic instability could occur in rotating RCE *if* there were TCLVs of size significantly larger than the deformation radius L_d. Baroclinic instability has a shortwave cutoff near the deformation radius, which is $2.6L_d$ in the classic Eady problem [*Vallis*, 2006, chap. 6]. Baroclinic instability does not disturb the growth of TCLVs of scales smaller than L_d due to self-aggregation of convection. But further growth of TCLVs past scales around L_d could be constrained by baroclinic instability.

6. Tropical Circulation in Rotating RCE

Another interesting aspect of the large-scale flow in rotating RCE is the existence of a pair of weak "Hadley cells" in the mass stream function of the zonal mean circulation (Figure 10), accompanied by Ferrel cell-like circulations in the subtropical region. The zonal wind field (Figure 11) is dominated by upper tropospheric easterlies extending into the subtropics in the stratosphere, with weak subtropical westerlies near the surface.

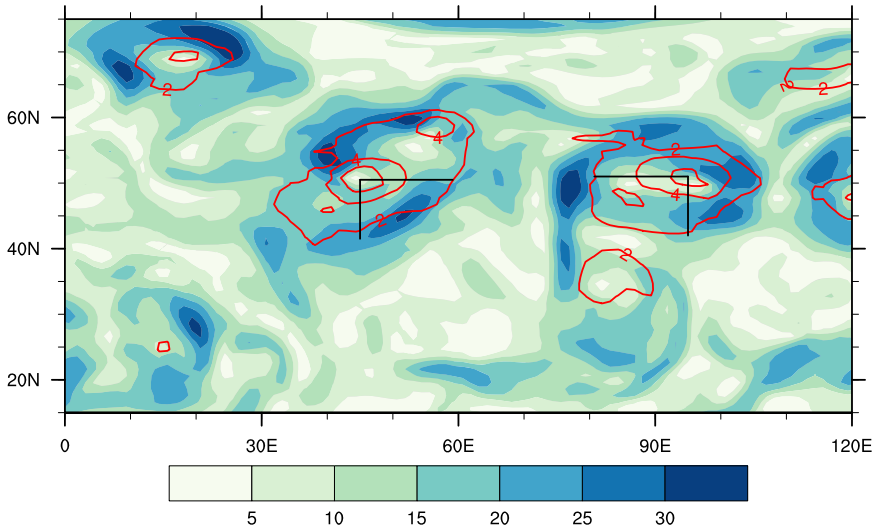

Figure 9. A snapshot of the differential wind speed between 250 and 850 hPa (color, in m s^{-1}) and anomalously temperature field at 500 hPa (contours with 2 K intervals). Black lines are 1000 km long, drawn for indicating the length scale in north-south or east-west direction of the map.

Previous GCM simulations of rotating RCE have also been found to develop a Hadley circulation. The weak Hadley circulation in our simulation is very similar to the one found in one experiment of *Kirtman and Schneider* [2000, Figure 7], in which an AGCM is coupled to a mixed layer ocean model of constant 50 m depth, and the incident solar flux is prescribed to be constant globally. This similarity suggests that the absence of incident solar radiation and a coupled mixed layer ocean are not crucial in determining the general characteristics of the large-scale circulation in a rotating RCE state.

The zonal mean precipitation (not shown) has weak minima of about 4.7 mm/d in the 10° bands around 15°N and 15°S, compared to about 5.7 mm/d poleward to 25° latitude and near the equator. This contrast is similar to the aforementioned simulation by Kirtman and Schneider, but the overall precipitation is higher because the radiative cooling of the atmosphere is stronger due to the lack of shortwave absorption in our nocturnal simulations.

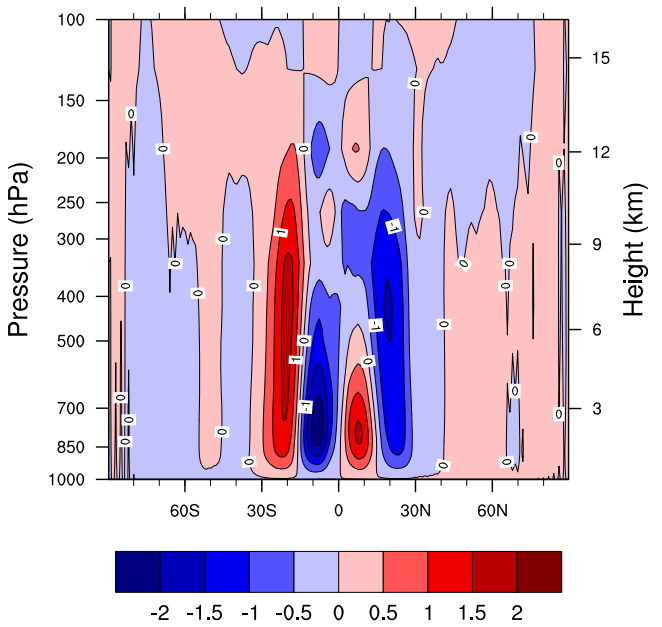

Figure 10. Mass stream function of the zonal mean circulation. The unit of contours is 10^{10} kg s^{-1}.

An eastward propagating convectively coupled equatorial Kelvin wave develops at the equator. The signal is most prominent in surface pressure field, which shows slowly eastward propagating high and low anomalies tied to anomalously low and high precipitation, respectively. Figure 12 plots the symmetric component of the power spectrum of surface pressure between 15°S and 15°N in wave number frequency domain, following

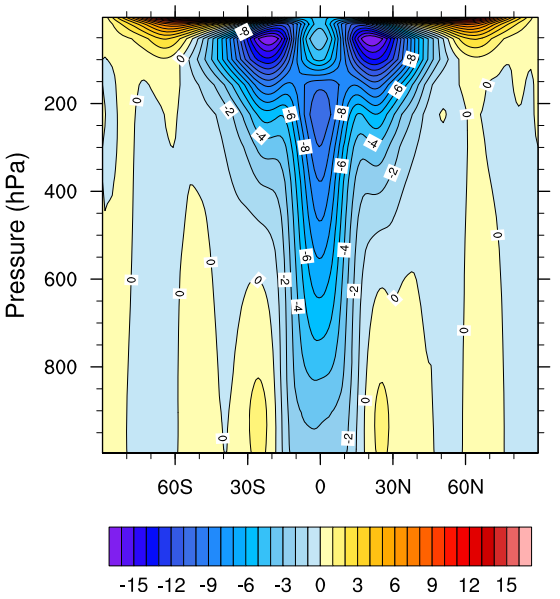

Figure 11. Zonal mean zonal wind in m s^{-1}.

the approach described by *Wheeler and Kiladis* [1999]. A Kelvin wave-like mode with wave number 1 and a period of about 30 days is prominent. We did not normalize the spectrum by its "background power spectrum," although doing so would not undermine the importance of this wave number 1 signal. This eastward propagating wave number 1 mode shares a similar period with the Madden-Julian Oscillation (MJO) [*Madden and Julian*, 1972, 1994], though it may be simply a convectively coupled Kelvin wave signal.

7. Momentum Transport and the Hadley Circulation

As *Kirtman and Schneider* [2000] documented, the formation of tropical easterlies and subtropical westerlies implies a net poleward transport of angular momentum in rotating RCE. They speculated that the poleward transport of angular momentum was accomplished by large-scale zonally asymmetric convective events and tested that by conducting a simulation with their GCM truncated to be zonally symmetric. However, in the zonally symmetric model, they still got an ITCZ, which transited between 20°N and 20°S with a 22 month period, and the angular momentum transport associated with this ITCZ was accomplished by eddies rather than the mean flow.

The results of *Kirtman and Schneider* [2000] highlighted the role of eddies in maintaining the Hadley circulation in rotating RCE. The zonally averaged and vertically integrated zonal momentum equation may be written as

$$\begin{aligned}\int \frac{\partial [u]}{\partial t}\frac{dp}{g} &= \int [v](f+[\zeta])\frac{dp}{g} - \int \frac{1}{a\cos^2\theta}\frac{\partial}{\partial \theta}\left(\cos^2\theta [u'v']\right)\frac{dp}{g} + \tau_x \\ &= \int [v] f \frac{dp}{g} + \int [v][\zeta]\frac{dp}{g} + \int M\frac{dp}{g} + \tau_x,\end{aligned} \tag{8}$$

where the square brackets represent zonal averages, prime denotes the deviation from zonal means, M denotes the convergence of zonal momentum transport of eddies, and τ_x is surface wind stress in zonal direction.

In (8), the $[v]f$ integral disappears if we average the equation in time because of mass conservation with every latitude circle in the steady state. So in rotating RCE, only the last three terms can contribute to the meridional transport of momentum. Taking simulation data between 5°S and 5°N, we can calculate each term in (8) and their time averages, so as to estimate the importance of each term in maintaining the Hadley circulation in rotating RCE. Normalizing them by surface pressure, the time averages are -1.8×10^{-4}, -1.1×10^{-2}, -0.19, $0.20\,\mathrm{ms^{-1}day^{-1}}$ for each of the four terms on the right side of (8), respectively. This confirms that the easterlies of the Hadley circulation in rotating RCE are driven by eddies. The contribution from mean circulation due to the integral of $[v][\zeta]$ is much smaller than eddy contribution since u' and v' are often significantly larger than $[u]$ and $[v]$.

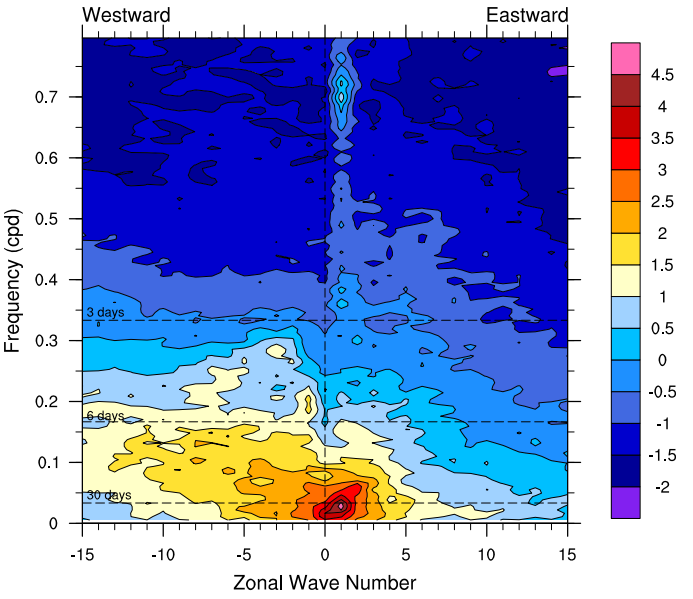

Figure 12. The symmetric component of the wave number frequency power spectrum of surface pressure between 15°S and 15°N.

Why do spontaneously generated convective vortices generate a momentum flux diverging away from the equator? This may be understood as a result of the strong vorticity stirring in the extratropics, but not near the equator, due to TCLVs, following *Vallis* [2006, chapter 12.1.2.III], which produces net wave activity flux into the tropics, and momentum flux out of it. Since the horizontal winds in TCLVs have a strong barotropic component, and (8) is vertically averaged, we idealize the flow to be barotropic. Kinematically, the momentum flux convergence is equal to the northward vorticity flux

$$M=-\frac{1}{a\cos^2\theta}\frac{\partial}{\partial\theta}\left(\cos^2\theta[u'v']\right)=[v'\zeta']. \tag{9}$$

Using a barotropic vorticity equation with sources F_ζ and sinks D_ζ, linearized about a mean flow with a positive meridional absolute vorticity gradient, $\Lambda=\beta-\partial^2[u]/\partial y^2$, Vallis formulates an pseudomomentum equation for Rossby wave activity density (which is proportional to vorticity variance). In steady state, it takes the following form:

$$[v'\zeta']=\frac{1}{\Lambda}\left([\zeta'F'_\zeta]-[\zeta'D'_\zeta]\right). \tag{10}$$

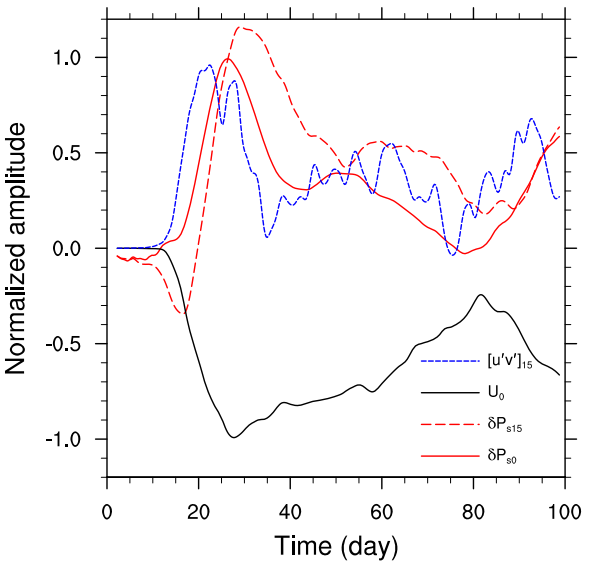

Figure 13. Vertically averaged zonal mean zonal wind (U_0) at the equator, and zonal mean surface pressure anomalies (δP_{s0} and δP_{s15}) at the equator and 15°N. The vertically averaged zonal mean eddy momentum flux at 15°N ($[u'v']_{15}$) is also plotted. The numbers in subscripts indicate latitudes. Surface pressure anomaly is the deviation of surface pressure from the globally uniform initial value. U_0 is normalized by $\max(|U_0|)=9.2\text{ms}^{-1}$, and δP_{s0} and δP_{s15} are normalized by $\max(\delta P_{s0})=4.0$ hPa for the purpose of plotting.

The eddy vorticity flux $[v'\zeta']$ is determined by the right-hand side of (10), which vanishes if the equation is integrated over latitude. Since there is stronger vorticity stirring by TCLVs in the extratropics than near the equator, the vorticity variance source should be larger there, while the sink due to dissipation may extend further into the equatorial belt. Hence, $[v'\zeta']$ is positive in the extratropics and negative within the tropics, which means there must be momentum flux convergence in the extratropics and divergence near the equator. This argument also applies to the eddy momentum transport into the eddy-driven jets on the real Earth. Its validity for

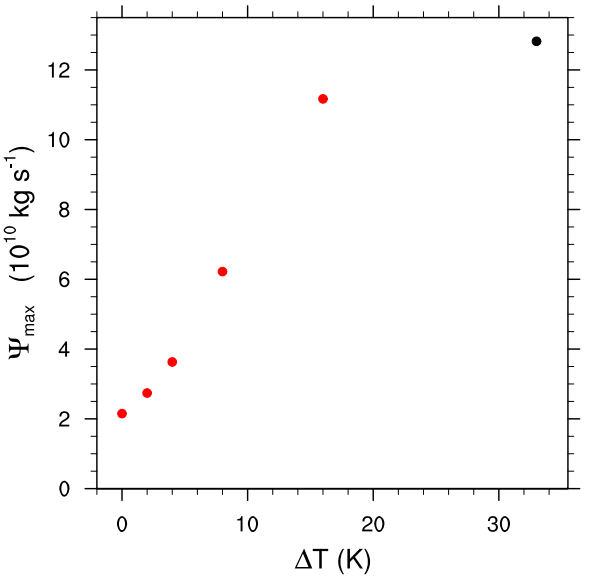

Figure 14. Hadley circulation intensity of simulations with different equator-to-pole temperature difference. The black dot indicates an aquaplanet simulation with observed zonal mean SST profile.

the rotating RCE case is still somewhat uncertain, since it relies on linear wave arguments based on excitation of Rossby waves in the vorticity stirring region, which propagate into the equatorial region before they dissipate, while highly nonlinear TCLVs dominate the flow at all latitudes in rotating RCE. Hence, a northward flux of vorticity variance in the TCLVs could also contribute to (10).

The role of eddy momentum fluxes in inducing the Hadley circulation can be clearly seen from the initial spin-up of rotating RCE from a state of rest. Figure 13 shows the time series of vertically averaged zonal mean zonal wind and zonal mean surface pressure fluctuation at 0° and 15°N, together with that of the vertically averaged zonal mean eddy momentum flux at 15°N, in the first 100 days of the simulation.

Prior to about day 10, the zonal mean variables have not yet changed much. In this stage, eddies are developing but are not yet well-formed. At about day 10, eddy momentum flux at 15°N starts to increase. Momentum flux divergence accelerates equatorial easterly. The momentum fluxes maximize at 20 days before settling back down to an irregular statistical steady state, and the equatorial zonal winds maximize about 5 days later. The surface pressure field gestrophically adjusts to support the evolving wind field. The pressure rises over the tropics and lowers over the poles to support the developing subtropical westerlies being accelerated by eddy stirring. Initially, these westerlies extend equatorward of 15°N/S and the surface pressure at 15°N/S drops, but then the Hadley circulation broadens as it strengthens and after day 25, the pressure is higher at 15°N/S than at the equator. Once an equatorial low forms, low-level convergence develops and finally leads to the emergence of Hadley cells.

Therefore, the emergence of Hadley cell in rotating RCE starts with a quiescent atmosphere followed by eddy transport of zonal momentum, which sets up tropical easterlies and subtropical westerlies. The simultaneous geostrophic adjustment away from the equator results in a meridional gradient in the pressure field, which in turn promotes the formation of Hadley cells.

How strong is this eddy-driven Hadley cell compared with the Hadley circulation on Earth? To answer this question, we conducted a series of simulations with increasing equator-to-pole SST gradient. The SST field is set by the following expression:

$$\mathrm{SST} = 300 - \Delta T \frac{\cos(\varphi) - 1}{2}, \tag{11}$$

where ΔT in K is the temperature difference between the equator and the pole. We conducted simulations with $\Delta T = 2, 4, 8, 16$ K. The intensity of Hadley cells is measured by the maximum of the mass stream function (Ψ_{max}) of the zonally averaged flow between 30°S and 30°N. The calculation result is shown in Figure 14, in which the result from an aquaplanet simulation with observed zonal mean SST profile is also compared.

As the equator-to-pole temperature difference increases, the Hadley cells become stronger and wider. The intensity of the Hadley circulation in rotating RCE is roughly 1/5 of its counterpart in the real world. Thus, while the Hadley cells are generally weak, they are not weak enough to be neglected.

The simple angular momentum conserving model developed by *Held and Hou* [1980] is a special approximate idealized model of the Hadley circulation that ignores the effects of eddies. It predicts that the intensity of the Hadley circulation is proportional to $\Delta\theta^{5/2}$, where $\Delta\theta$ is the change in vertically averaged potential temperature from pole to the equator. By comparing the simulations with $\Delta T = 2, 4, 8, 16$ K, which is roughly the same as $\Delta\theta$ in our simulations, we find that the intensity of Hadley circulations in Figure 14 does not increase as fast as the Held and Hou model predicts. Furthermore, the Hadley circulation does not vanish when ΔT becomes zero. These discrepancies underscore the fundamental role of eddies in the formation of Hadley cells, consistent with what *Walker and Schneider* [2005] suggested in their study on the response of Hadley circulation to seasonally varying heating.

8. Conclusions

Building on simulations by *Held and Zhao* [2008] of RCE on a large doubly periodic *f* plane, a slightly more complicated rotating RCE simulation on a sphere is achieved by prescribing globally uniform SST and eliminating incident solar radiation in a global atmospheric model. In this rotating RCE on a sphere, as in Held and Zhao's simulations, moist convection aggregates into a population of long-lived tropical cyclone-like vortices.

TCLVs are generated in the subtropical region, then move poleward and westward, due to the effect of beta drift. Many of those TCLVs can travel to high latitudes near the pole, in an average time of about 2 months. The mean spacing of mature TCLVs in the extratropics is approximately 2 times the deformation radius L_d.

The energy spectrum of atmosphere in rotating RCE is quite similar to that of the Earth's atmosphere, with a k^{-3} spectral slope at scales smaller than the deformation radius, and relatively flat spectrum at scale larger than the deformation radius. In both cases, these spectral features result from the concentration of APE production near the scale of the deformation radius, but the production mechanism in rotating RCE is the latent heating in the warm cores of the TCLVs, while on the real earth, it is baroclinic instability ultimately driven by equator-to-pole temperature differences.

An inspection of the temperature gradient between the warm cores of TCLVs and surrounding regions and the associated vertical wind shear suggests that baroclinic instability can break up TCLVs of size significantly larger than the deformation radius L_d. The combination of self-aggregation and baroclinic instability helps limit the spacing of TCLVs to about $2L_d$ in rotating RCE.

A weak eddy-driven Hadley circulation develops in our simulation of rotating RCE, similar to previous studies. Its strength is about 1/5 that of its real-world counterpart. A Kelvin wave-like mode with wave number 1 and a period of 30–40 days is found at the equator.

The presence of a weak Hadley circulation and the beta drift of TCLVs enrich the dynamics of rotating RCE on a sphere, yet do not appear to increase the complexity in an overwhelming way. Such a rotating RCE simulation with spherical geometry, together with other variants of rotating RCE, may help us understand how the TCs simulated in GCMs depends upon environment parameters and parameterization schemes in an idealized manner, in addition to allowing us to understand the minimal set of factors needed to support-related dynamical phenomena in the real atmosphere.

Acknowledgments
The authors acknowledge support from the National Science Foundation (NSF) Center for Multiscale Modeling of Atmospheric Processes (CMMAP; grant ATM-0425247). The first author is also supported in part by NSF grant AGS-1138977. Computing was done on the Hyak supercomputer system, supported in part by the University of Washington eScience Institute. All data used in this analysis are available upon request.

References

Anderson, J. L., et al. (2004), The new GFDL global atmosphere and land model AM2–LM2: Evaluation with prescribed SST simulations, *J. Clim.*, *17*(24), 4641–4673, doi:10.1175/JCLI-3223.1.

Augier, P., and E. Lindborg (2013), A new formulation of the spectral energy budget of the atmosphere, with application to two high-resolution general circulation models, *J. Atmos. Sci.*, *70*(7), 2293–2308, doi:10.1175/JAS-D-12-0281.1.

Bretherton, C. S., P. N. Blossey, and M. Khairoutdinov (2005), An energy-balance analysis of deep convective self-aggregation above uniform SST, *J. Atmos. Sci.*, *62*(12), 4273–4292, doi:10.1175/JAS3614.1.

Chan, J. C. L., and R. T. Williams (1987), Analytical and numerical studies of the beta-effect in tropical cyclone motion. Part I: Zero mean flow, *J. Atmos. Sci.*, *44*(9), 1257–1265, doi:10.1175/1520-0469(1987)044⟨1257:AANSOT⟩2.0.CO;2.

Gage, K. S., and G. D. Nastrom (1986), Theoretical interpretation of atmospheric wavenumber spectra of wind and temperature observed by commercial aircraft during gasp, *J. Atmos. Sci.*, *43*(7), 729–740.

Hartmann, D. L., and K. Larson (2002), An important constraint on tropical cloud-climate feedback, *Geophys. Res. Lett.*, *29*(20), 1951, doi:10.1029/2002GL015835.

Held, I. M., and A. Y. Hou (1980), Nonlinear axially symmetric circulations in a nearly inviscid atmosphere, *J. Atmos. Sci.*, *37*(3), 515–533, doi:10.1175/1520-0469(1980)037⟨0515:NASCIA⟩2.0.CO;2.
Held, I. M., and M. Zhao (2008), Horizontally homogeneous rotating radiative-convective equilibria at GCM resolution, *J. Atmos. Sci.*, *65*(6), 2003–2013, doi:10.1175/2007JAS2604.1.
Khairoutdinov, M., and K. Emanuel (2013), Rotating radiative-convective equilibrium simulated by a cloud-resolving model, *J. Adv. Model. Earth Syst.*, *5*(4), 816–825, doi:10.1002/2013MS000253.
Kirtman, B. P., and E. K. Schneider (2000), A spontaneously generated tropical atmospheric general circulation, *J. Atmos. Sci.*, *57*(13), 2080–2093, doi:10.1175/1520-0469(2000)057⟨2080:ASGTAG⟩2.0.CO;2.
Li, X., and B. Wang (1994), Barotropic dynamics of the beta gyres and beta drift, *J. Atmos. Sci.*, *51*(5), 746–756.
Lin, S.-J. (2004), A "vertically Lagrangian" finite-volume dynamical core for global models, *Mon. Weather Rev.*, *132*(10), 2293–2307, doi:10.1175/1520-0493(2004)132⟨2293:AVLFDC⟩2.0.CO;2.
Madden, R. A., and P. R. Julian (1972), Description of global-scale circulation cells in the tropics with a 40–50 day period, *J. Atmos. Sci.*, *29*(6), 1109–1123, doi:10.1175/1520-0469(1972)029⟨1109:DOGSCC⟩2.0.CO;2.
Madden, R. A., and P. R. Julian (1994), Observations of the 40–50-day tropical oscillation—A review, *Mon. Weather Rev.*, *122*(5), 814–837, doi:10.1175/1520-0493(1994)122⟨0814:OOTDTO⟩2.0.CO;2.
Manabe, S., and R. F. Strickler (1964), Thermal equilibrium of the atmosphere with a convective adjustment, *J. Atmos. Sci.*, *21*(4), 361–385, doi:10.1175/1520-0469(1964)021⟨0361:TEOTAW⟩2.0.CO;2.
Moorthi, S., and M. J. Suarez (1992), Relaxed Arakawa-Schubert: A parameterization of moist convection for general circulation models, *Mon. Weather Rev.*, *120*(6), 978–1002, doi:10.1175/1520-0493(2000)128⟨1070:ASFCOT⟩2.0.CO;2.
Muller, C. J., and I. M. Held (2012), Detailed investigation of the self-aggregation of convection in cloud-resolving simulations, *J. Atmos. Sci.*, *69*(8), 2551–2565, doi:10.1175/JAS-D-11-0257.1.
Nolan, D. S., and E. D. Rappin (2008), Increased sensitivity of tropical cyclogenesis to wind shear in higher SST environments, *Geophys. Res. Lett.*, *35*, L14805, doi:10.1029/2008GL034147.
Nolan, D. S., E. D. Rappin, and K. A. Emanuel (2007), Tropical cyclogenesis sensitivity to environmental parameters in radiative–convective equilibrium, *Q. J. R. Meteorol. Soc.*, *133*(629), 2085–2107.
Robe, F. R., and K. A. Emanuel (1996), Moist convective scaling: Some inferences from three-dimensional cloud ensemble simulations, *J. Atmos. Sci.*, *53*(22), 3265–3275, doi:10.1175/1520-0469(1996)053⟨3265:MCSSIF⟩2.0.CO;2.
Romps, D. M. (2011), Response of tropical precipitation to global warming, *J. Atmos. Sci.*, *68*(1), 123–138, doi:10.1175/2010JAS3542.1.
Rotstayn, L. D. (1997), A physically based scheme for the treatment of stratiform clouds and precipitation in large-scale models. I: Description and evaluation of the microphysical processes, *Q. J. R. Meteorol. Soc.*, *123*(541), 1227–1282, doi:10.1002/qj.49712354106.
Rotstayn, L. D., B. F. Ryan, and J. J. Katzfey (2000), A scheme for calculation of the liquid fraction in mixed-phase stratiform clouds in large-scale models, *Mon. Weather Rev.*, *128*(4), 1070–1088, doi:10.1175/1520-0493(2000)128⟨1070:ASFCOT⟩2.0.CO;2.
Salmon, R. (1978), Two-layer quasi-geostrophic turbulence in a simple special case, *Geophys. Astrophys. Fluid Dyn.*, *10*(1), 25–52, doi:10.1080/03091927808242628.
Salmon, R. (1980), Baroclinic instability and geostrophic turbulence, *Geophys. Astrophys. Fluid Dyn.*, *15*(1), 167–211, doi:10.1080/03091928008241178.
Sumi, A. (1992), Pattern formation of convective activity over the aqua-planet with globally uniform sea surface temperature (SST), *J. Meteorol. Soc. Jpn.*, *70*(5), 855–876.
Tompkins, A. M., and G. C. Craig (1998), Radiative-convective equilibrium in a three-dimensional cloud-ensemble model, *Q. J. R. Meteorol. Soc.*, *124*(550), 2073–2097, doi:10.1002/qj.49712455013.
Vallis, G. K. (2006), *Atmospheric and Oceanic Fluid Dynamics: Fundamentals and Large-Scale Circulation*, Cambridge Univ. Press, Cambridge, U. K.
Walker, C. C., and T. Schneider (2005), Response of idealized Hadley circulations to seasonally varying heating, *Geophys. Res. Lett.*, *32*, L06813, doi:10.1029/2004GL022304.
Wang, B., and X. Li (1992), The beta drift of three-dimensional vortices: A numerical study, *Mon. Weather Rev.*, *120*, 579–593.
Wang, Y., and G. Holland (1996), The beta drift of baroclinic vortices. Part I: Adiabatic vortices, *J. Atmos. Sci.*, *53*(3), 411–427.
Wheeler, M., and G. N. Kiladis (1999), Convectively coupled equatorial waves: Analysis of clouds and temperature in the wavenumber-frequency domain, *J. Atmos. Sci.*, *56*(3), 374–399, doi:10.1175/1520-0469(1999)056⟨0374:CCEWAO⟩2.0.CO;2.
Zhao, M., I. M. Held, S.-J. Lin, and G. A. Vecchi (2009), Simulations of global hurricane climatology, interannual variability, and response to global warming using a 50-km resolution GCM, *J. Atmos. Sci.*, *22*(24), 6653–6678.
Zhou, W., I. M. Held, and S. T. Garner (2014), Parameter study of tropical cyclones in rotating radiative-convective equilibrium with column physics and resolution of a 25 km GCM, *J. Atmos. Sci.*, *71*, 1058–1069, doi:http://dx.doi.org/10.1175/JAS-D-13-0190.1.
Zurita-Gotor, P., and G. K. Vallis (2009), Equilibration of baroclinic turbulence in primitive equations and quasigeostrophic models, *J. Atmos. Sci.*, *66*(4), 837–863, doi:10.1175/2008JAS2848.1.